Computers and Mathematics with Applications 96 (2021) 209–228

Contents lists available at ScienceDirect

Computers and Mathematics with Applications

journal homepage: www.elsevier.com/locate/camwa

Workpiece-scale numerical simulations of SLM molten pool dynamic behavior of 316L stainless steel

Liu Cao

Advanced Institute of Engineering Science for Intelligent Manufacturing, Guangzhou University, Guangzhou 510006, Guangdong, China

ARTICLE INFO

Article history:
Available online 5 May 2020

Keywords:
Selective laser melting
Molten pool dynamic behavior
Equivalent processing model
Two-phase flow model
316L stainless steel
Numerical simulation

ABSTRACT

316L stainless steel is currently one of the most critical stainless-steel materials due to its excellent corrosion resistance and comprehensive mechanical properties. Selective laser melting (SLM), as an additive manufacturing technology for directly forming complex metal parts, has been applied in the production of 316L stainless steel components. By introducing reasonable and comprehensive equivalent processing models (e.g., gasification pressure, gasification heat dissipation, and equivalent physical parameters), a predictive model of the dynamic behavior of the molten pool on the workpiece scale (two-phase flow model) was established for the SLM process of 316L stainless steel. The related equivalent processing models were customized by secondary development means based on the commercial software Fluent. By comparing and analyzing the different calculation schemes, it was found that surface tension stabilizes the liquid metal surface, while the Marangoni effect and the gasification recoil force cause the liquid metal surface to appear concave. The tangential movement of the liquid metal surface, caused by the Marangoni effect, causes the molten metal to accumulate around the central region, forming a liquid surface morphology resembling a crater. The influence of different processing parameters (scanning speed and laser power) on the SLM process of 316L stainless steel was analyzed. The simulated and experimentally obtained solidified track sizes were in good agreement.

1. Introduction

316L stainless steel is currently one of the most critical stainless-steel materials due to its excellent corrosion resistance and comprehensive mechanical properties, and it is widely used in many products, including pipelines, chemicals, heat exchangers, and molds [1]. However, with the increasing demands on component structures (such as industrial precision molds with conformal cooling channels), traditional 316L stainless steel smelting, forging, and material reduction processing methods (such as CNC machine tools) have gradually become inadequate to meet the growing processing requirements for the fabrication of complex parts. Additive manufacturing technology is a "bottom-up" production method for stacked materials, which can quickly produce complex parts [2]. Selective laser melting (SLM), as a major technical approach in metal additive manufacturing, has been widely used in automotive, aerospace, dental and other fields [3] (Fig. 1).

In recent years, scholars have carried out many experimental studies on SLM of 316L stainless steel powder, mainly involving the observation of SLM process, and the influences of process parameters on the microstructure and mechanical

E-mail address: caoliu@gzhu.edu.cn.

https://doi.org/10.1016/j.camwa.2020.04.020
0898-1221/

Nomenclature

$\overline{\rho}$, ρ_1, ρ_2	Mixed, metal-phase, and gas-phase densities, respectively (kg/m^3)
$\boldsymbol{u}$	Velocity (m/s)
t	Time (s)
$\otimes$	Tensor product
p	Pressure (Pa)
$\overline{\tau}$	Stress tensor
g	Gravitational acceleration (m/s^2)
$\boldsymbol{F}_{buoyancy}$	Buoyancy (N/m^3)
$\boldsymbol{F}_{mushy}$	Mushy zone drag force (N/m^3)
$\boldsymbol{F}_{tension}$	Surface tension (N/m^2)
$\boldsymbol{F}_{Marangoni}$	Marangoni force (N/m^2)
F_{recoil}	Gasification recoil force of liquid metal (N/m^2)
α_1, α_2	Volume ratios of metal and gas phases, respectively
$\overline{\mu}$, μ_1, μ_2	Mixed, metal-phase, and gas-phase dynamic viscosities, respectively (Pa s)
β	Thermal expansion coefficient (1/K)
T	Temperature (K)
T_{ref}	Thermal expansion reference temperature (K)
K_C	Porous media permeability coefficient (1/s)
C_K	A custom small value, such as 1e−2
f_l	Liquid ratio of metal phase
σ	Surface tension coefficient (N/m)
κ	Gas–liquid interface curvature (1/m)
$\boldsymbol{n}$	Gas–liquid interface unit normal vector (pointing from gas phase to metal phase)
$d\sigma/dT$	Rate of change of σ with temperature (N/(m K))
p_{vap}	Gasification pressure of liquid metal (Pa)
p_{amb}	Protective atmosphere pressure (Pa)
$\overline{c}_e$, c_{p1}, c_{p2}	Equivalent, metal-phase, and gas-phase specific heat capacities, respectively (J/(kg K))
L_f	Metal melting latent heat (J/kg)
T_l, T_s	Metal liquidus and solidus temperatures, respectively (K)
$\overline{k}$, k_1, k_2	Mixed, metal-phase, and gas-phase thermal conductivities, respectively (W/(m K))
q_{con}	Convective heat dissipation (W/m^2)
h_{con}	Convective heat transfer coefficient (W/(m^2 K))
T_{con}	Outside temperature at gas–liquid interface (K)
q_{rad}	Radiant heat dissipation (W/m^2)
σ_s	Stefan–Boltzmann constant (W/(m^2 K^4))
ε	Emissivity
T_{rad}	External radiation temperature (K)
q_{vap}	Gasification heat dissipation of liquid metal (W/m^2)
Q_{laser}	Laser energy density (W/m^3)
W_{laser}	Laser power (W)
ξ	Energy distribution factor
η	Effective absorption factor
χ	Ratio of central energy density of lower end face to upper end face
z_e, z_i	Height coordinates of upper and lower end faces of laser energy distribution area (m)
r_e, r_i	Radius of upper and lower end faces of laser energy distribution area (m)
r_0	Laser distribution cross-section radius corresponding to height coordinate z (m)
w, s, E, F	Calculation intermediates
$\dot{m}_{vap}$	Gasification mass of liquid metal on unit liquid surface per unit time (kg/(m^2 s))
ΔH_{vap}	Metal gasification latent heat (J/kg)
m	Metal molecular mass (kg)
k_B	Boltzmann constant (J/K)
p_0	Standard atmospheric pressure (Pa)

T_v	Metal gasification temperature (K)
T_{left}, T_{right}	Left and right critical temperatures of transition zone (K)
p_{smooth}	Transition zone pressure (Pa)
β_r	Recombination rate
ρ_e	Equivalent density (kg/m^3)
ϕ	Initial porosity of powder layer
k_e	Equivalent thermal conductivity (W/(m K))
k_r	Thermal conductivity for characterizing internal radiation of powder layer (W/(m K))
F_{view}	Internal radiation factor
T_P	Temperature of metal particle (K)
D_P	Average particle diameter (m)

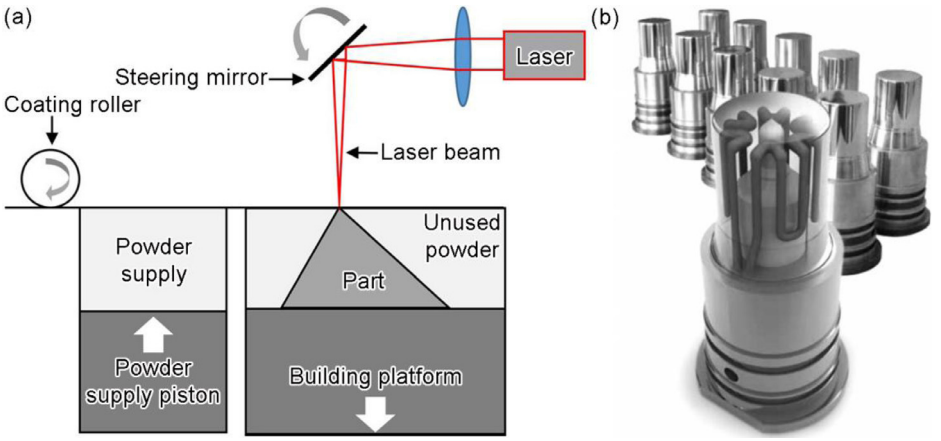

Fig. 1. SLM technology and its typical application: (a) SLM schematic; (b) industrial precision mold with conformal cooling channels printed by SLM.

properties of parts [4–6]. Cherry et al. [7] investigated the effect of the volumetric energy density on 316L stainless steel properties during the SLM process. The point distance and exposure time were varied, and their impact on the porosity, surface finish, microstructure, density, and hardness were evaluated. The surface roughness was primarily affected by the point distance – an increased point distance resulted in an increased surface roughness – and the material hardness was related to the material's porosity. Liu et al. [8] performed single-track SLM experiments to observe the spatter behavior using a high-speed camera. The influence of the energy input on the spatter behavior was investigated by employing 316L stainless steel powder. The results indicated that the energy input affected the size, scattering state, and jetting height of the spatter. The above experimental research results have important value for understanding the process of SLM of 316L stainless steel powder. However, because the SLM process is in a rapidly changing high temperature environment, it is difficult to quantitatively analyze the characteristic data of the SLM process, such as the change in the depth of the molten pool over time. As a typical quantitative analysis method, numerical simulation has gradually become a powerful tool for studying the SLM process [9,10].

At present, the numerical simulation research on SLM process is mainly divided into two aspects: based on the particle scale [11,12], and based on the workpiece scale [13,14]. The so-called particle scale refers to the geometric modeling of the actual morphology of the powder bed particles, and then to calculate the complex interaction between the laser beam and the metal particles [15]. It mainly involves the research contents of spreading powder [16,17], laser heat source [18], and molten pool dynamics [19,20]. Zheng et al. [19] proposed a novel physical model for SLM, providing insights into the surface morphology evolution in the pulsed SLM process. Both Marangoni effect and recoil pressure, which were the prevailing driving forces for the melt flow, were incorporated in the model. The disadvantage of the particle-scale simulation research is that the calculation efficiency is low, because the mesh size is often at the micron level and the time step is at the microsecond level [21]. The so-called workpiece scale refers to the powder bed as a continuous phase, and then the equivalent thermophysical parameters and equivalent flow behavior model are used to describe the SLM process. It is mainly used to obtain the change of the temperature and size of the molten pool with time during the forming process [22,23]. Bruna-Rosso et al. [24] proposed a finite element model of the SLM process, and reduced melt pool geometries were simulated in the first tracks which led to lack of fusion defect. The advantage of the workpiece-scale simulation research is that it requires less computing resources to describe the SLM process by equivalent methods, which makes its calculation efficiency high [25]. But these simulation studies have adopted single-phase flow model to

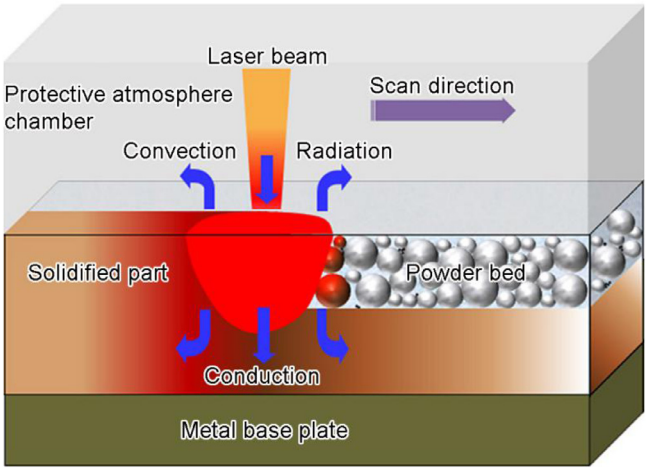

Fig. 2. Schematic of SLM process.

calculate the evolution process of the molten pool and have failed to describe the phenomenon of the liquid metal surface fluctuations during the SLM process [22–25].

In this paper, by introducing reasonable and comprehensive equivalent processing models (e.g., gasification pressure, gasification heat dissipation, and equivalent physical parameters), a dynamic behavior prediction model of the SLM molten pool based on the workpiece scale (two-phase flow model) was established for the SLM process of 316L stainless steel. The secondary development method was used to customize the relevant equivalent processing models based on Fluent, and a numerical simulation of the SLM process of 316L stainless steel was carried out. To illustrate the effects of surface tension, the Marangoni effect, and the gasification recoil force on the dynamic behavior of the molten pool, the calculation results with and without the surface tension and the Marangoni effect included were considered. Next, the effects of different process parameters (e.g., laser power and scanning speed) on the SLM process of 316L stainless steel were calculated and compared with the experimental results.

2. Mathematical and numerical modeling

2.1. Dynamic behavior control equations of SLM molten pool based on the workpiece scale

Fig. 2 shows the schematic of SLM process. During the calculation, the powder bed was melted by the laser beam, and then gradually solidified. In addition, the following three assumptions were adopted here: the mass loss caused by metal liquid gasification was not considered, the effect of metal density changes on the volume was not considered, and the fluids were considered to be incompressible, Newtonian fluids.

2.1.1. Momentum conservation equation

When metal particles are melted by laser radiation, factors affecting the flow behavior of the liquid metal include the surface tension between the liquid metal and the protective gas, the Marangoni effect (due to the surface tension gradient caused by the temperature difference on the liquid metal surface under the laser's active area), the gasification recoil force of the liquid metal, buoyancy, the internal pressure of the liquid metal, internal viscous forces of the liquid metal, gravity, and the difference in the fluidities between the liquid and solid metal during solidification. The first three influencing factors are surface forces, and the last five influencing factors are volumetric forces. To fully consider the various factors affecting the dynamic behavior of the molten pool during the SLM process, the model used herein was a two-phase flow model and, based on the Navier–Stokes equations [26], the momentum conservation equation is as follows:

$$\begin{aligned}&\frac{\partial \overline{\rho}\boldsymbol{u}}{\partial t}+\nabla\cdot(\overline{\rho}\boldsymbol{u}\otimes\boldsymbol{u})=-\nabla p+\nabla\cdot\overline{\tau}+\overline{\rho}\boldsymbol{g}+\boldsymbol{F}_{buoyancy}+\boldsymbol{F}_{mushy}\\&+\left(\boldsymbol{F}_{tension}+\boldsymbol{F}_{Marangoni}+\boldsymbol{F}_{recoil}\right)|\nabla\alpha_1|\frac{2\overline{\rho}}{\rho_1+\rho_2}f_l\alpha_1\end{aligned}\tag{1}$$

where

$$\overline{\rho}=\alpha_1\rho_1+\alpha_2\rho_2\tag{2}$$

$$\overline{\tau}=2\overline{\mu}\left[\left(\frac{1}{2}\nabla\boldsymbol{u}+\frac{1}{2}(\nabla\boldsymbol{u})^T\right)-\frac{1}{3}(\nabla\cdot\boldsymbol{u})\mathbf{I}\right]\tag{3}$$

$$\overline{\mu} = \alpha_1\mu_1 + \alpha_2\mu_2 \tag{4}$$

$$\boldsymbol{F}_{buoyancy} = \overline{\rho}\boldsymbol{g}\beta\left(T - T_{ref}\right) \tag{5}$$

$$\boldsymbol{F}_{mushy} = -\alpha_1\overline{\rho}K_C\left[\frac{(1-f_l)^2}{f_l^3 + C_K}\right]\boldsymbol{u} \tag{6}$$

$$\boldsymbol{F}_{tension} = \sigma\kappa\boldsymbol{n} \tag{7}$$

$$\boldsymbol{F}_{Marangoni} = \frac{d\sigma}{dT}\left[\nabla T - \boldsymbol{n}\left(\boldsymbol{n}\cdot\nabla T\right)\right] \tag{8}$$

$$\boldsymbol{F}_{recoil} = \left(p_{vap} - p_{amb}\right)\boldsymbol{n} \tag{9}$$

$$\boldsymbol{n} = \frac{\nabla\alpha_1}{|\nabla\alpha_1|} \tag{10}$$

$$\kappa = -\nabla\cdot\boldsymbol{n} \tag{11}$$

$\boldsymbol{F}_{mushy}$ can be used to characterize the difference in the fluidity caused by the liquid–solid transition [27]. $\boldsymbol{F}_{tension}$ is calculated using the CSF (continuum surface force) model [28]. $\boldsymbol{F}_{Marangoni}$ is used to characterize the Marangoni effect (because the laser energy density is Gaussian in the horizontal plane, the temperature on the liquid metal surface is high in the center and lower in the surrounding area; the surface tension is related to temperature, and thus, liquid metal flow occurs on the surface under the influence of the surface tension gradient [29]). K_C is used to characterize the extent to which the mushy zone affects the flow, as the mushy zone can be considered to be a special porous medium, and the value of K_C used herein was 1.0, which was derived from the recommended value of software Fluent. C_K is used to prevent the drag force of the mushy zone from becoming infinite during the calculation (when f_l is zero). In addition, the purpose of $|\nabla\alpha_1|$ in the rightmost term of Eq. (1) is to make the surface forces (surface tension, Marangoni effect, and gasification recoil force) equivalent to the volume forces, and the purpose of $\frac{2\overline{\rho}}{\rho_1+\rho_2}f_l\alpha_1$ is to obtain a smooth force distribution near the liquid metal surface. The calculation of p_{vap} will be explained in Section 2.3.

The volume ratio factor of the metal phase α_1 is used to indicate the volume fraction of the metal phase at different locations, where a value of 1 indicates that the mesh element is completely occupied by the metal phase, a value of 0 indicates that it is completely occupied by the gas phase, and a value between 0 and 1 is at the interface. The equation governing α_1 is the volume ratio equation (volume of fluid algorithm) [30]:

$$\frac{\partial\alpha_1}{\partial t} + \nabla\cdot(\alpha_1\boldsymbol{u}) = 0 \tag{12}$$

$$\alpha_1 + \alpha_2 = 1 \tag{13}$$

2.1.2. Energy conservation equation

The factors to be considered in the calculation of the temperature field of the SLM process include the absorption of the laser energy, melting of the solid metal, gasification of the liquid metal, convection and diffusion inside the metal phase, and heat exchange between the metal phase and the surroundings (convection and radiation). The energy conservation equation is as follows:

$$\frac{\partial\overline{\rho}\overline{c}_eT}{\partial t} + \nabla\cdot(\overline{\rho}\boldsymbol{u}\overline{c}_eT) = \nabla\cdot\left(\overline{k}\nabla T\right) - \left[\left(q_{con} + q_{rad} + q_{vap}\right)|\nabla\alpha_1| - Q_{laser}\right]\frac{2\overline{\rho}\overline{c}_e}{\rho_1c_{p1} + \rho_2c_{p2}} \tag{14}$$

where

$$\overline{c}_e = \begin{cases} \alpha_1\left(c_{p1} + \dfrac{L_f}{T_l - T_s}\right) + \alpha_2c_{p2} & T_l < T < T_s \\ \alpha_1c_{p1} + \alpha_2c_{p2} & T \geq T_l \text{ or } T \leq T_s \end{cases} \tag{15}$$

$$\overline{k} = \alpha_1k_1 + \alpha_2k_2 \tag{16}$$

$$q_{con} = h_{con}\left(T - T_{con}\right) \tag{17}$$

$$q_{rad} = \sigma_s\varepsilon\left(T^4 - T_{rad}^4\right) \tag{18}$$

The expression for $\overline{c}_e$ was obtained from a previous report [31]. In addition, the purpose of $|\nabla\alpha_1|$ in Eq. (14) is to equalize the surface heat dissipation (convection, radiation, and gasification heat dissipation) and the body heat dissipation, and the purpose of $\frac{2\overline{\rho}\overline{c}_e}{\rho_1c_{p1}+\rho_2c_{p2}}$ is to obtain a smooth heat dissipation distribution near the liquid metal surface.

2.1.3. Mass conservation equation

Since the fluids involved were considered incompressible in the calculation process, the mass conservation equation is as follows:

$$\nabla\cdot\boldsymbol{u} = 0 \tag{19}$$

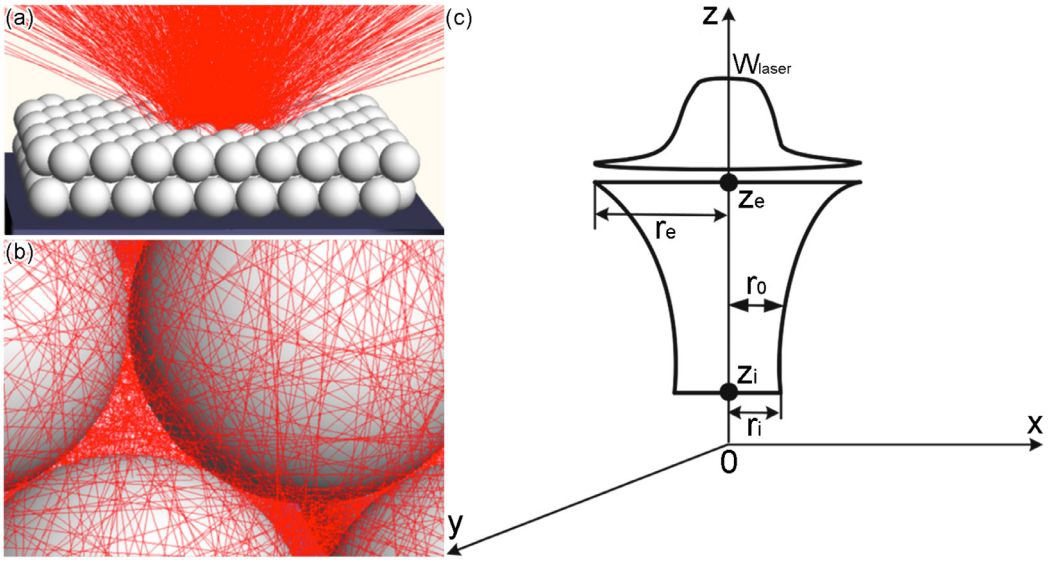

Fig. 3. Schematic of Gaussian body heat source: (a, b) laser transmission between particles; (c) energy density distribution of body heat source.

2.2. Gaussian body heat source considering laser reflection between particles

The laser energy model used here was a Gaussian body heat source [23,32]. Fig. 3 shows the schematic of the energy density distribution of the body heat source. The mathematical expression is as follows:

$$Q_{laser} = \frac{\xi \eta W_{laser}}{\pi \left(1 - e^{-3}\right)(E + F)} \left(\frac{1 - \chi}{z_e - z_i} z + \frac{\chi z_e - z_i}{z_e - z_i}\right) \exp\left(-\frac{3r^2}{r_0^2}\right) \tag{20}$$

where

$$r_0 = \frac{z^2}{w} + s \tag{21}$$

$$w = \frac{z_e^2 - z_i^2}{r_e - r_i} \tag{22}$$

$$s = \frac{r_i z_e^2 - r_e z_i^2}{z_e^2 - z_i^2} \tag{23}$$

$$E = \frac{1 - \chi}{z_e - z_i} \left\{ \left(\frac{1}{w^2} \frac{z_e^6}{6} + \frac{s}{w} \frac{z_e^4}{2} + \frac{s^2}{2} z_e^2 \right) - \left(\frac{1}{w^2} \frac{z_i^6}{6} + \frac{s}{w} \frac{z_i^4}{2} + \frac{s^2}{2} z_i^2 \right) \right\} \tag{24}$$

$$F = \frac{\chi z_e - z_i}{z_e - z_i} \left\{ \left(\frac{1}{w^2} \frac{z_e^5}{5} + 2 \frac{s}{w} \frac{z_e^3}{3} + s^2 z_e \right) - \left(\frac{1}{w^2} \frac{z_i^5}{5} + 2 \frac{s}{w} \frac{z_i^3}{3} + s^2 z_i \right) \right\} \tag{25}$$

2.3. Gasification pressure and heat dissipation model

For general metals, the gasification temperature is around 3000 K. The laser beam has a very high energy density during the SLM process, and it is often able to vaporize the metal in a very short time. Therefore, an accurate SLM simulation must account for the effects of the gasification heat dissipation and the gasification recoil force. The calculation model of gasification heat dissipation [33] used in this study is as follows:

$$q_{vap} = \alpha_1 \dot{m}_{vap} \Delta H_{vap} \tag{26}$$

where

$$\dot{m}_{vap} = \left(p_{vap} - p_{amb}\right) \sqrt{\frac{m}{2\pi k_B T}} \tag{27}$$

The role of α_1 in Eq. (26) was to ensure that the gasification heat dissipation of the gas-phase element was zero, and the role of $p_{vap} - p_{amb}$ in Eq. (27) was to ensure that the gasification heat dissipation was zero when the element temperature was lower than the gasification temperature.

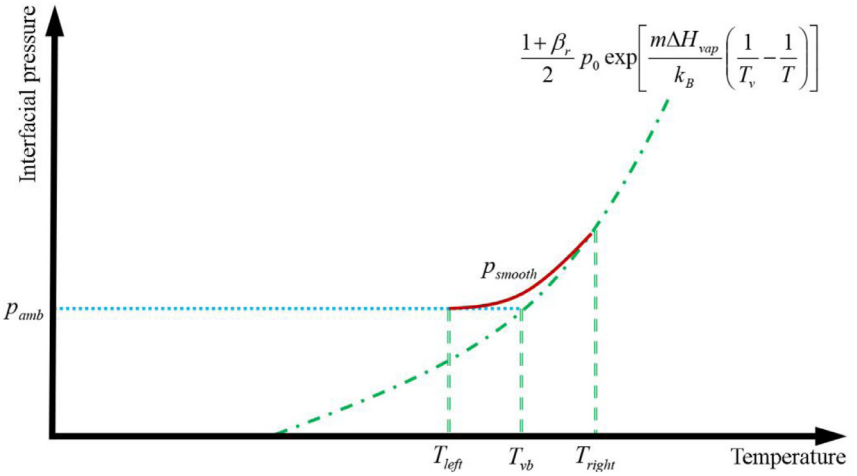

Fig. 4. Schematic of gasification pressure model.

The calculation of p_{vap} uses the gasification pressure model for different environmental pressures proposed by Pang et al. [34]:

$$p_{vap} = \begin{cases} p_{amb} & 0 \le T < T_{left} \\ \dfrac{1+\beta_r}{2} p_0 \exp\left[\dfrac{m\Delta H_{vap}}{k_B}\left(\dfrac{1}{T_v}-\dfrac{1}{T}\right)\right] & T \ge T_{right} \\ p_{smooth} & T_{left} \le T < T_{right} \end{cases} \tag{28}$$

The value of β_r depends on the Mach number of the vapor plume. For high gasification rate conditions (such as under a vacuum or at a high laser intensity), $\beta_r = 0.18$, and for low gasification rate conditions (such as under a high ambient pressure or at a low laser intensity), $\beta_r = 1$. In other cases, the value of β_r is between the two.

The purpose of setting the transition zone is to avoid the sharp discontinuous first derivative of p_{vap}, to ensure the stability of the numerical solution. The function of the transition zone pressure, p_{smooth}, is to achieve a smooth interfacial pressure over the entire temperature range (Fig. 4). The intersecting temperature, T_{vb}, in Fig. 4 can be calculated by the following formula:

$$\frac{1+\beta_r}{2} p_0 \exp\left[\frac{m\Delta H_{vap}}{k_B}\left(\frac{1}{T_v}-\frac{1}{T_{vb}}\right)\right] = p_{amb} \tag{29}$$

Once T_{vb} is determined, the left and right critical temperatures of the transition zone, T_{left}, T_{right}, were set as follows:

$$T_{right} - T_{vb} = T_{vb} - T_{left} = 0.075 T_{vb} \tag{30}$$

To obtain a smooth transition, the form of p_{smooth} was artificially selected as:

$$p_{smooth} = aT^3 + bT^2 + cT + d \tag{31}$$

To ensure a smooth transition of the interface pressure at T_{left} and T_{right}, the distribution of p_{smooth} can be obtained based on the coordinates of the two ends and the slopes of the tangents.

2.4. Equivalent thermal property parameter based on formation state

The core of the numerical simulation based on the workpiece scale is to select an equivalent special material to represent the powder layer. However, in the actual SLM process, the powder layer undergoes a process of melting into liquid metal and becoming a dense solid. Therefore, the powder layer can be considered to undergo transitions between three state: particle, liquid, and solid states. In the calculation process, the basis for judging whether the state of the powder layer has changed is as follows: (1) once the temperature of the original particle element exceeds its melting temperature (generally taken as the intermediate value of the liquidus and solidus temperature), the element state is converted to a liquid state; (2) for elements that are originally in the liquid or solid state, their state will only change between liquid and solid (based on the liquidus–solidus temperature of the metal). The equivalent physical properties (density, specific heat capacity, and thermal conductivity) based on the formation state of the powder layer (particle, liquid, and solid states) are described below.

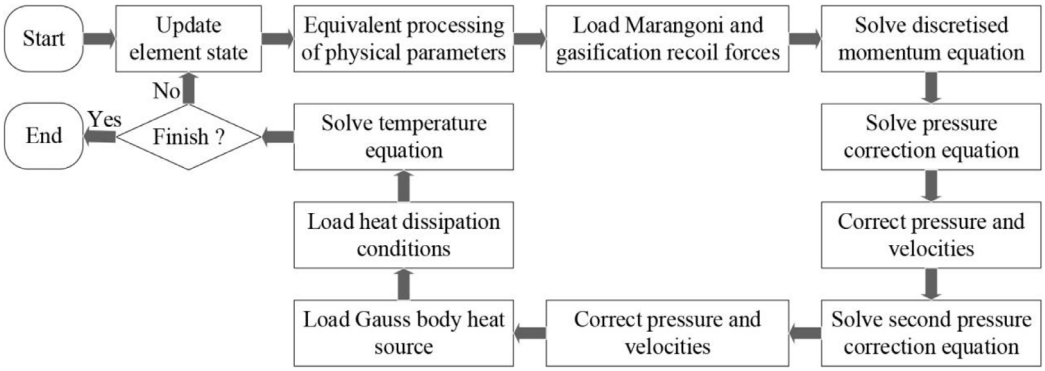

Fig. 5. Calculation flow chart.

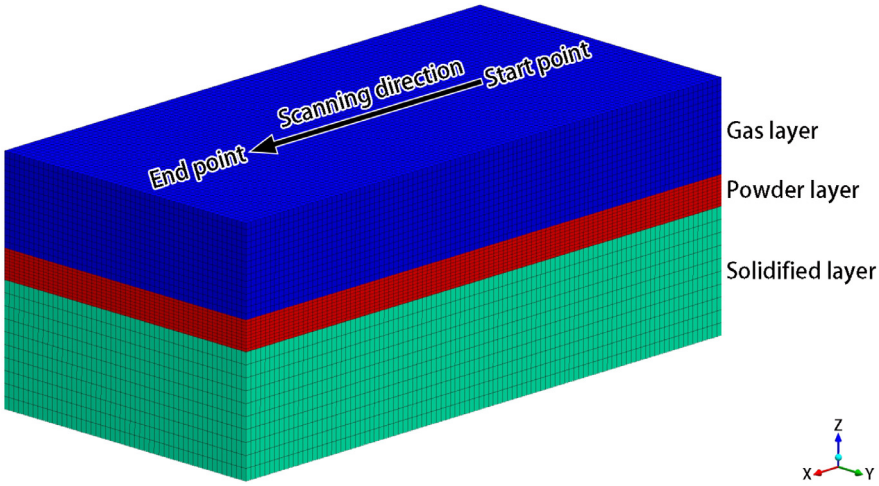

Fig. 6. Adopted geometry and mesh models (black lines were split lines of meshes). (For interpretation of the references to color in this figure legend, the reader is referred to the web version of this article.)

(1) Equivalent density and specific heat capacity based on formation state

During the calculation, the density of the powder layer element is expressed as follows:

$$\rho_e = \begin{cases} (1-\phi)\,\rho_1 + \phi\rho_2 & \textit{particle state} \\ \rho_1 & \textit{liquid state or solid state} \end{cases} \tag{32}$$

where ρ_1 and ρ_2 are temperature-dependent. The specific heat capacity of the powder layer element was expressed similarly.

(2) Equivalent thermal conductivity based on formation state

For the thermal conductivity of the powder layer, an expression similar to Eq. (32) cannot be used (the equivalent physical property parameter is the weighted average of the physical parameters of the constituent phases). For the powder layer element in the particle state, the thermal conductivity is mainly determined by the heat conduction of the gas phase between the particles, but it is also slightly affected by the thermal conductivity of the particles themselves. Thus, the equivalent thermal conductivity model [35] of the powder layer is as follows:

$$k_e = \begin{cases} \left(1-\sqrt{1-\phi}\right)(k_2+\phi k_r) + \sqrt{1-\phi}\left\{\dfrac{2}{\frac{1}{k_2}-\frac{1}{k_1}}\left[\dfrac{1}{1-\frac{k_2}{k_1}}\ln\left(\dfrac{k_1}{k_2}\right)-1\right]+k_r\right\} & \textit{particle state} \\ k_1 & \textit{liquid state or solid state} \end{cases} \tag{33}$$

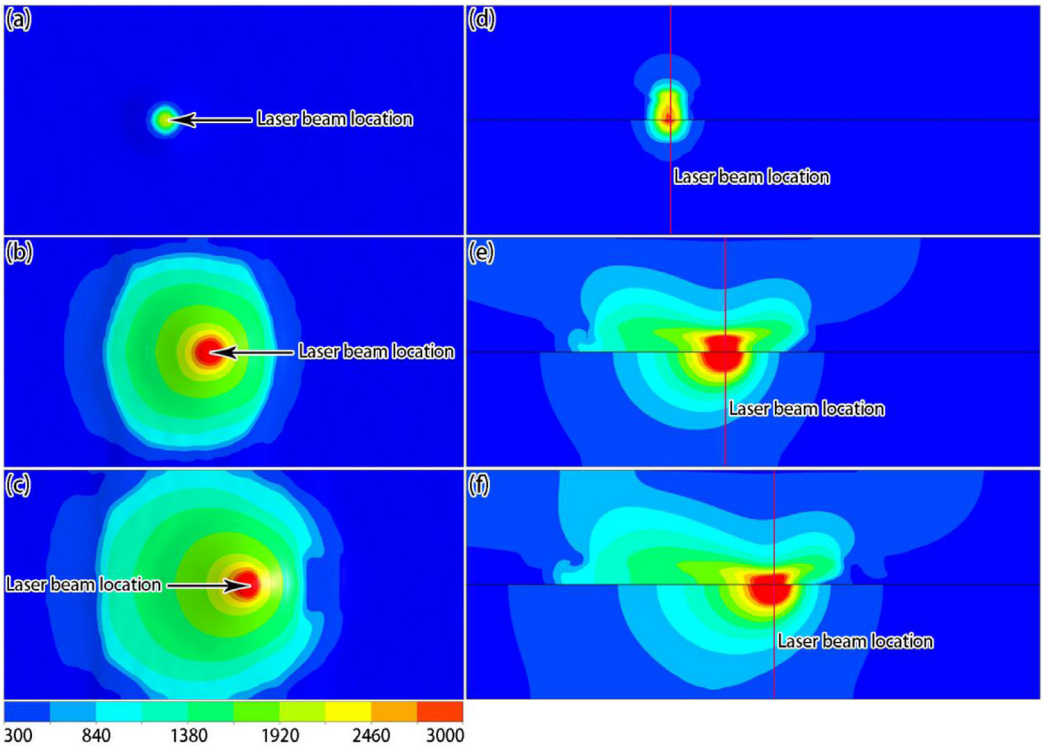

Fig. 7. Temperature calculation results of the liquid surface (a∼c) and the mid-section (d∼f) at different times in scheme A: (a, d) 3×10^{-5} s; (b, e) 1.02×10^{-3} s; and (c, f) 1.86×10^{-3} s (Unit: K).

where

$$k_r = 4F_{view}\sigma_s T_P^3 D_P \tag{34}$$

F_{view} is 1/3 [35], and k_1 and k_2 are temperature-dependent.

2.5. Numerical solution of dynamic behavior of SLM molten pool on workpiece scale

Using the commercial CFD software Fluent, a numerical calculation of the dynamic behavior of the SLM molten pool on the workpiece scale was carried out. The selected solution models were *Multiphase-Volume of Fluid*, *Energy*, *Viscous–Laminar*, and *Solidification & Melting*. The user defined functions (UDFs) included a moving Gaussian body heat source, equivalent physical parameters (density, specific heat capacity, and thermal conductivity), heat dissipation conditions (convection, radiation, and gasification), the Marangoni effect, and the gasification recoil force. To calculate the natural convection inside the gas phase, the gas density was determined by the *Boussinesq* model. The pressure–velocity coupling algorithm was *SIMPLEC*, and the time step was 1 ns. Fig. 5 shows the calculation flow chart for this study.

3. Results and discussion

According to the above physical model and numerical solution, the dynamic behavior of a SLM molten pool on the workpiece scale was predicted using Fluent. Firstly, to illustrate the effects of the surface tension, the Marangoni effect, and the gasification recoil force on the dynamic behavior of the molten pool, the calculated results with and without the surface tension and Marangoni effect included were compared. Secondly, to analyze the effects of different process parameters (e.g., laser power and scanning speed) on the SLM process of 316L stainless steel, the dynamic behaviors of the SLM molten pool for different processes were calculated and compared with the actual solidified track sizes obtained in the SLM experiments completed by Masmoudi et al. [36]. The mesh generation tool was ICEM CFD, and CFD-Post was used for post-processing.

3.1. Calculation parameters and mesh model

The composition (mass percentage) of the 316 L stainless steel was as follows: Fe 65.395-C 0.03-Si 1.0-Mn 2.0-P 0.045-S 0.03-Ni 12.0-Cr 17.0-Mo 2.5. Table 1 shows the required 316 L stainless steel physical parameters, calculated by software JMatPro 7.0.

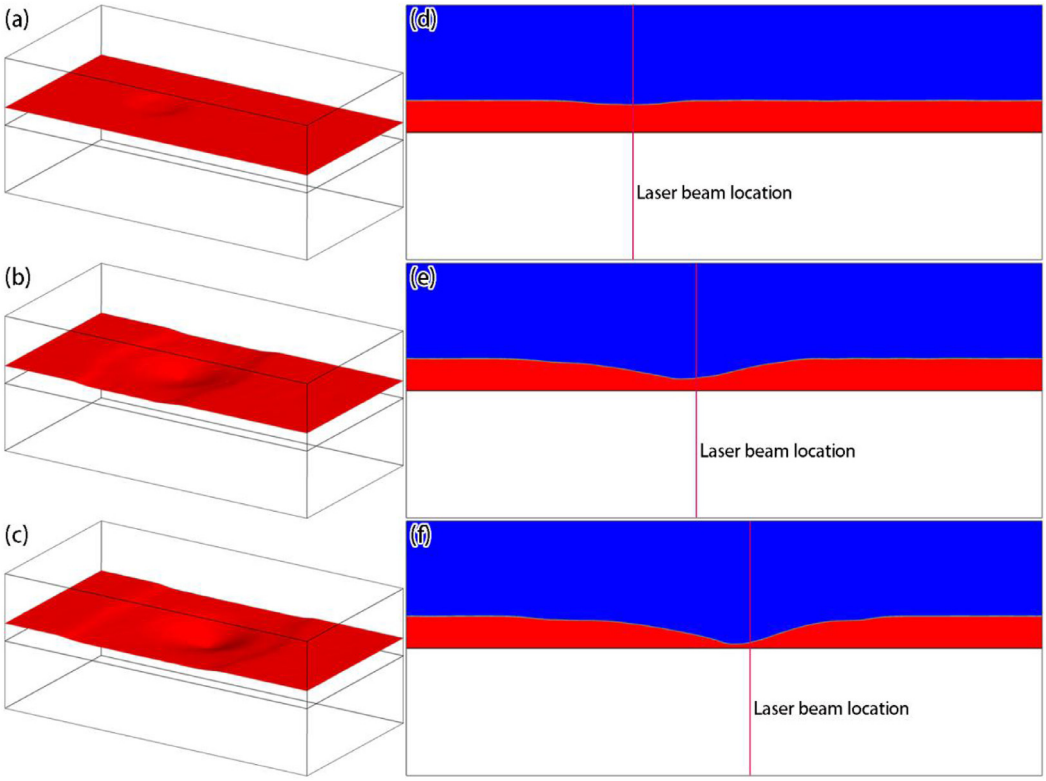

Fig. 8. Calculation results of the liquid surface fluctuation (a∼c) and the mid-section phase distribution (d∼f, red is metal phase, and blue is gas phase) at different times in scheme A: (a, d) 3×10^{-5} s; (b, e) 1.02×10^{-3} s; and (c, f) 1.86×10^{-3} s. (For interpretation of the references to color in this figure legend, the reader is referred to the web version of this article.)

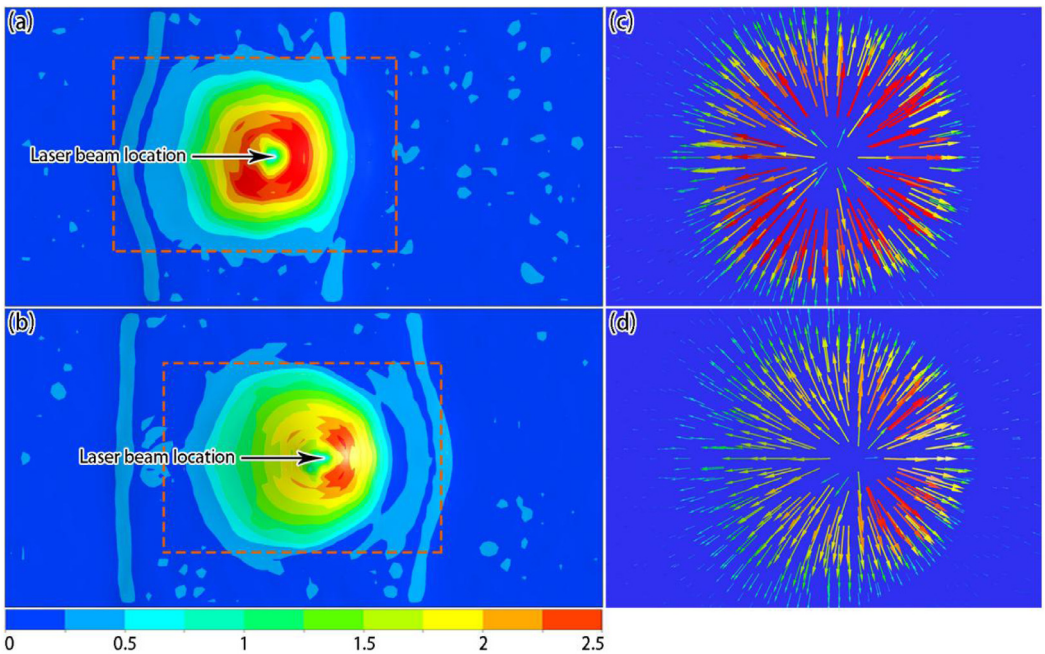

Fig. 9. Calculation results of the liquid surface speed (a, b) and the local velocity (c, d) at different times in scheme A: (a, c) 1.02×10^{-3} s; (b, d) 1.86×10^{-3} s (Unit: m/s).

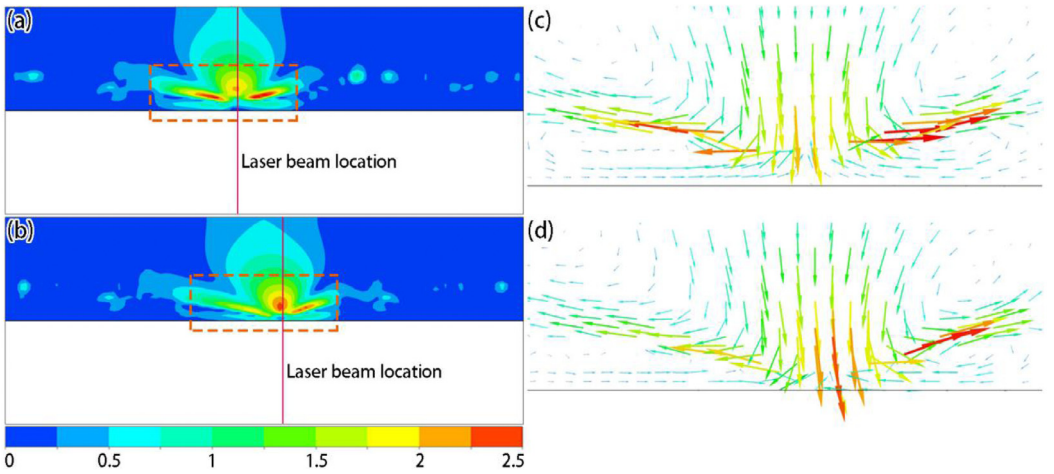

Fig. 10. Calculation results of the mid-section speed (a, b) and the local velocity (c, d) at different times in scheme A: (a, c) 1.02×10^{-3} s; (b, d) 1.86×10^{-3} s (Unit: m/s).

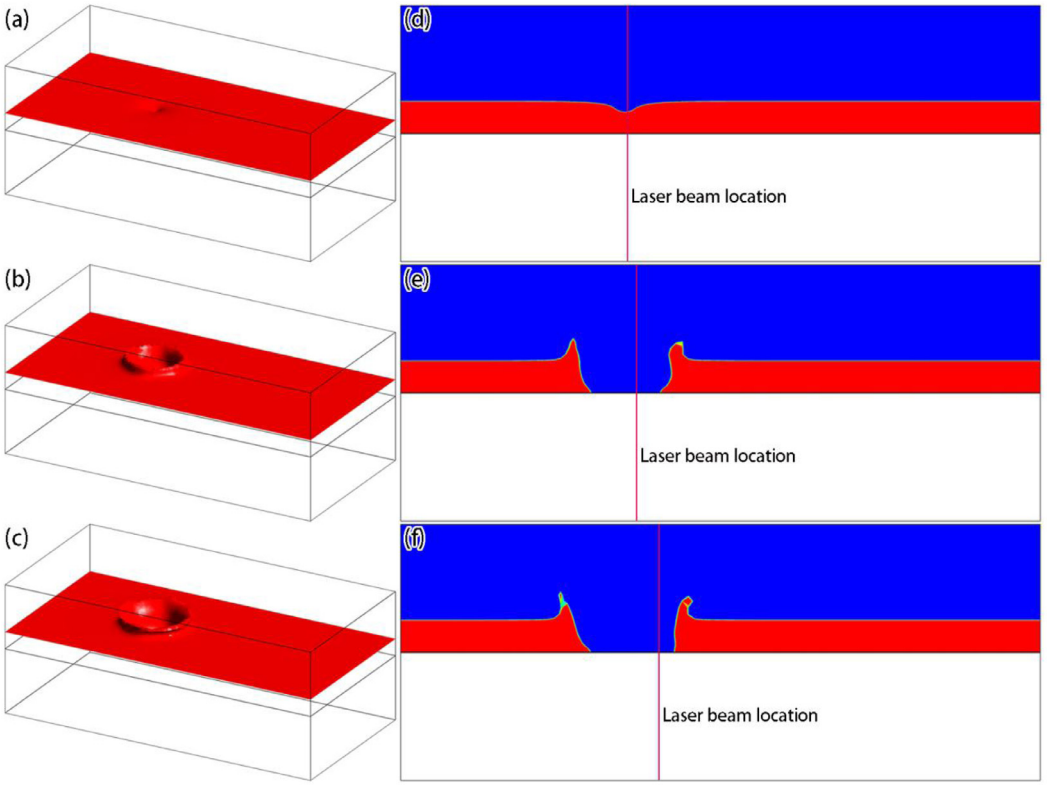

Fig. 11. Calculation results of the liquid surface fluctuation (a∼c) and the mid-section phase distribution (d∼f, red is metal phase, and blue is gas phase) at different times in scheme B: (a, d) 3×10^{-5} s; (b, e) 1.2×10^{-4} s; and (c, f) 5.1×10^{-4} s. (For interpretation of the references to color in this figure legend, the reader is referred to the web version of this article.)

The gasification pressure, p_{vap} (Pa), of the 316L stainless steel calculated according to Eqs. (28)–(31) was as follows:

$$p_{vap} = \begin{cases} 1.01325 \times 10^5 & 0 < T < 2950 \\ 1.964 \times 10^{-3} T^3 - 17.444 T^2 + 5.164 \times 10^4 T - 5.086 \times 10^7 & 2950 \le T < 3430 \\ 60795 \exp\left[50193 \times \left(\dfrac{1}{3090} - \dfrac{1}{T}\right)\right] & T \ge 3430 \end{cases} \tag{35}$$

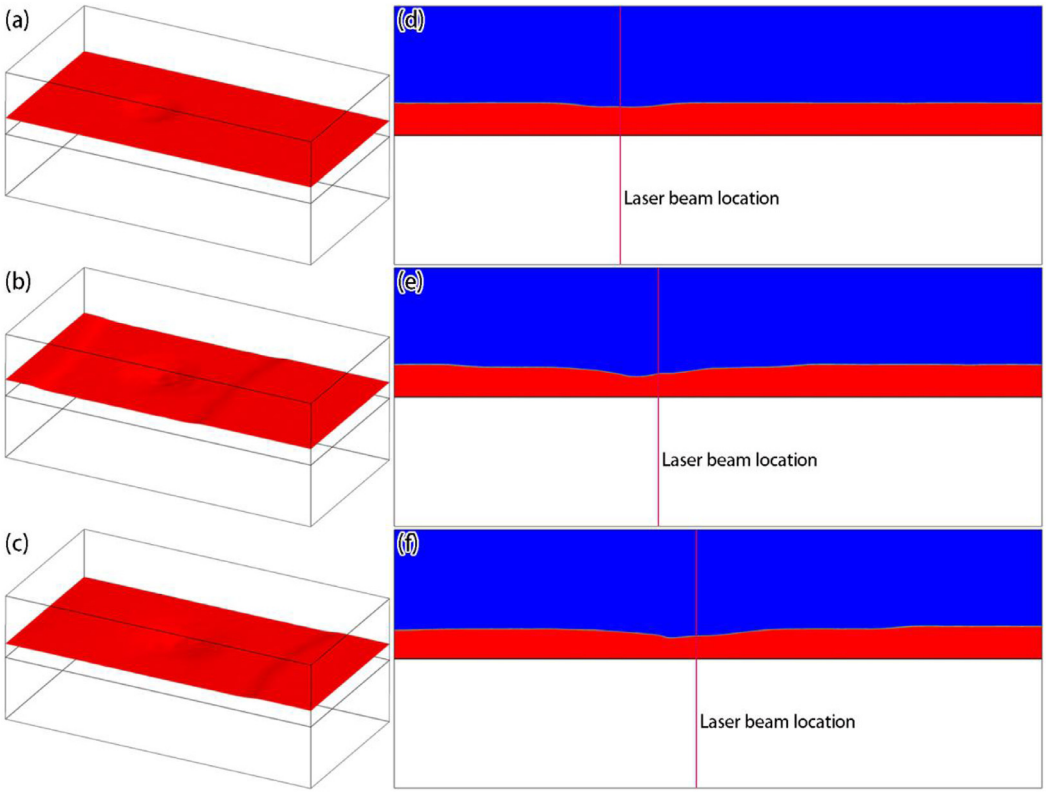

Fig. 12. Calculation results of the liquid surface fluctuation (a∼c) and the mid-section phase distribution (d∼f, red is metal phase, and blue is gas phase) at different times in scheme C: (a, d) 3×10^{-5} s; (b, e) 6×10^{-4} s; and (c, f) 1.2×10^{-3} s. (For interpretation of the references to color in this figure legend, the reader is referred to the web version of this article.)

Table 1
Physical parameters of 316L stainless steel.

Parameter	Value
Density (kg/m^3)	6130 (2773 K)-7050 (1708 K)-7220 (1658 K)-7300 (1568 K)-7350 (1493 K)-7660 (793 K)-7850 (298 K)
Solidus temperature (K)	1493
Liquidus temperature (K)	1708
Gasification temperature (K)	3090
Latent heat of melting (J/kg)	2.7×10^5
Latent heat of vaporization (J/kg)	7.45×10^6
Specific heat capacity (J/(kg· K))	755 (1600 K)-502 (298 K)
Surface tension coefficient (N/m)	1.76
Change rate of surface tension coefficient with temperature (N/(m· K))	-4.002×10^{-4}
Molecular mass (kg)	9.3692×10^{-26}
Thermal conductivity (W/(m· K))	46.33 (2773 K)-29.99 (1708 K)-32.56 (1668 K) -32.49 (1618 K)-31.12 (1493 K)-15.76 (298 K)
Dynamic viscosity (Pa· s)	0.00225 (2773 K)-0.0042 (2108 K)-0.00772 (1708 K)-0.00901 (1608 K)-0.01155 (1493 K)

The protective atmosphere in the experiment was argon, and the other parameters required for the calculation are shown in Table 2.

Fig. 6 shows the geometry and mesh model used in the simulation. The calculation area was divided into three parts: gas, powder, and solidified layers. The geometric dimensions of the three layers were $1 \times 0.5 \times 0.15$ mm^3, $1 \times 0.5 \times 0.05$ mm^3, and $1 \times 0.5 \times 0.2$ mm^3, respectively, and the corresponding mesh sizes were $0.01 \times 0.01 \times 0.01$ mm^3, $0.01 \times 0.01 \times 0.005$ mm^3, and $0.01 \times 0.01 \times 0.02$ mm^3. The corresponding numbers of mesh elements obtained were 75000, 50000, and 50000, respectively. The boundary conditions were as follows: the top surface of the gas layer was set as the pressure outlet boundary, the contact surface between the powder and solidified layers was set as a coupled wall, and the other boundary faces were assigned convective heat transfer conditions. In addition, the laser scanning start point,

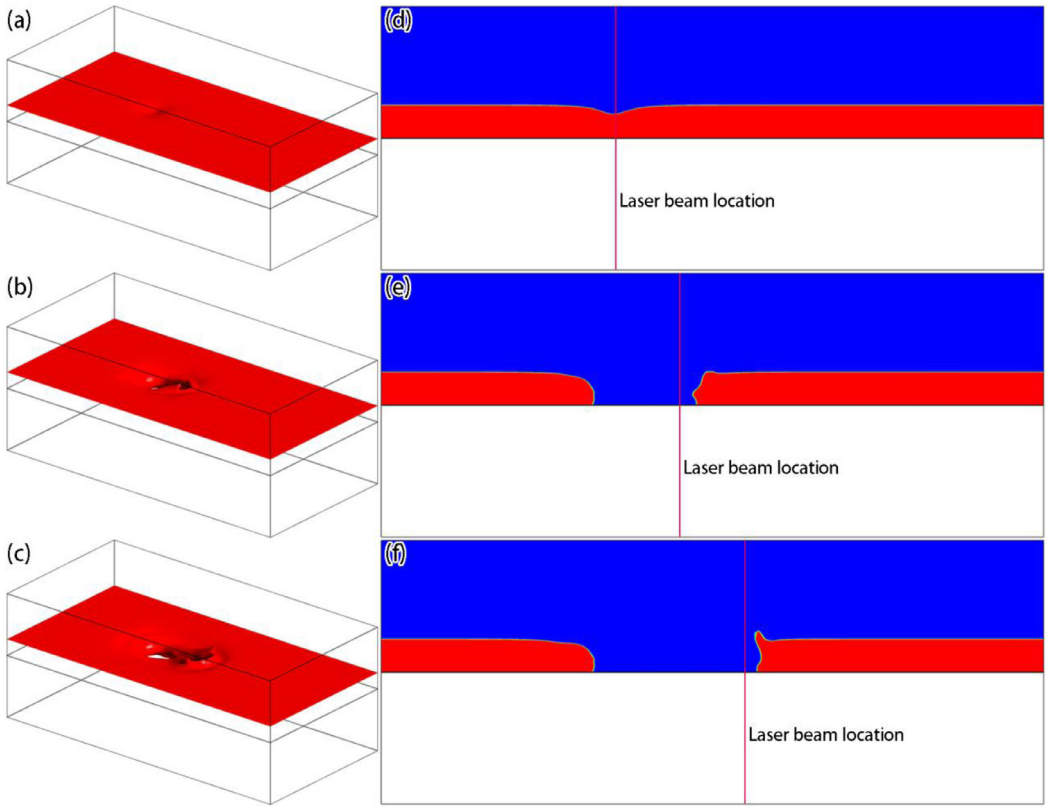

Fig. 13. Calculation results of the liquid surface fluctuation (a∼c) and the mid-section phase distribution (d∼f, red is metal phase, and blue is gas phase) at different times in scheme D: (a, d) 3×10^{-5} s; (b, e) 1.02×10^{-3} s; and (c, f) 2.01×10^{-3} s. (For interpretation of the references to color in this figure legend, the reader is referred to the web version of this article.)

Table 2
Other parameters required for calculation.

Parameter	Value
Initial porosity of powder layer	0.44
Density of gas phase (kg/m^3)	1.4
Specific heat capacity of gas phase (J/(kg K))	520
Thermal conductivity of gas phase (W/(m K))	0.01795
Dynamic viscosity of gas phase (Pa s)	2.2442×10^{-5}
Relative molecular mass of gas phase	39.94
Laser absorption ratio	0.3
Laser spot diameter (m)	6.8×10^{-5}
Average particle diameter (m)	3×10^{-5}
Powder bed thickness (m)	5×10^{-5}
Convective heat transfer/radiation outside temperature (K)	288
Convective heat transfer coefficient of lower surface of solidified layer (W/(m^2 K))	80
Emissivity	0.36
Initial temperature (K)	288
Stefan–Boltzmann constant (W/(m^2 K^4))	5.67×10^{-8}
Boltzmann constant (J/K)	$1.3806505 \times 10^{-23}$
Standard atmospheric pressure (Pa)	1.01325×10^5

end point, and scanning direction in the single-pass process are indicated in Fig. 6 (the x coordinates of the start and end points were 0.35 and 0.65 mm, respectively).

3.2. Effects of surface tension and marangoni effect on dynamic behavior of SLM molten pool

In order to analyze the influences of three factors (surface tension, Marangoni effect, and gasification recoil force) on the dynamic behavior of the molten pool, four calculation schemes were designed, as shown in Table 3. For the method

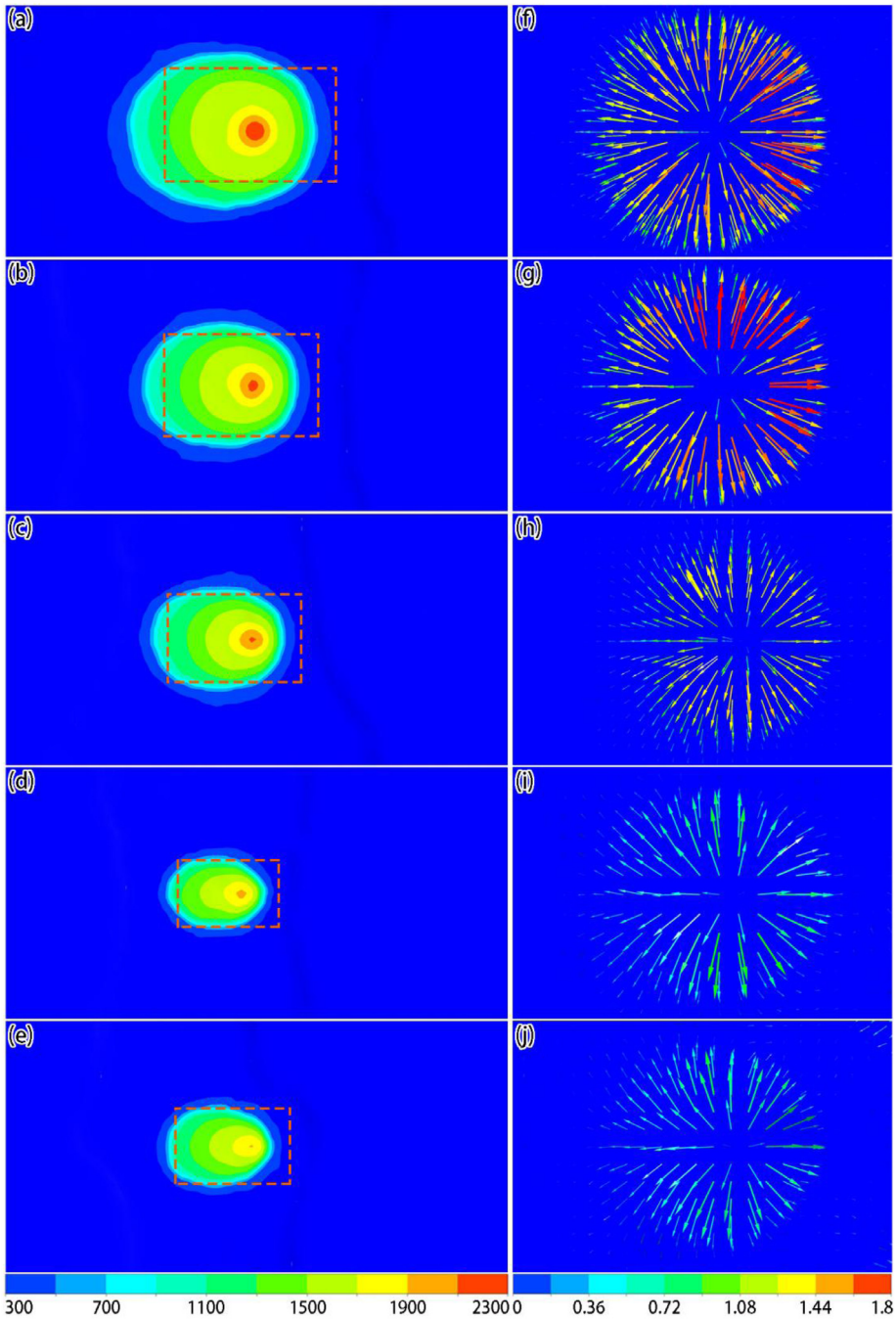

Fig. 14. The liquid surface temperature (a∼e, unit: K) and local velocity (f∼j, unit: m/s) distributions when the laser was applied to the center of the powder layer at different scanning speeds: (a, f) 0.1 m/s; (b, g) 0.2 m/s; (c, h) 0.3 m/s; (d, i) 0.4 m/s; and (e, j) 0.5 m/s.

in which the surface tension was neglected, the surface tension coefficient in *Phase Interaction* was set to 0 N/m. For the method in which the Marangoni effect was neglected, the change rate of surface tension coefficient with the temperature in the UDF file was set to 0 N/(m K).

Figs. 7 and 8 show the calculated temperature distribution and liquid surface morphology at different times in Scheme A. Since the laser energy density was Gaussian in the horizontal plane, the temperature at the center of the active laser region was high, and the surrounding temperature was low (Fig. 7a–c). When the powder layer element was in the particle state, its thermal conductivity was almost 1/1000 of that of the metal phase, and the heat was transmitted faster in the laser-application region (Fig. 7). As the temperature of the active laser region gradually increased, the molten metal surface

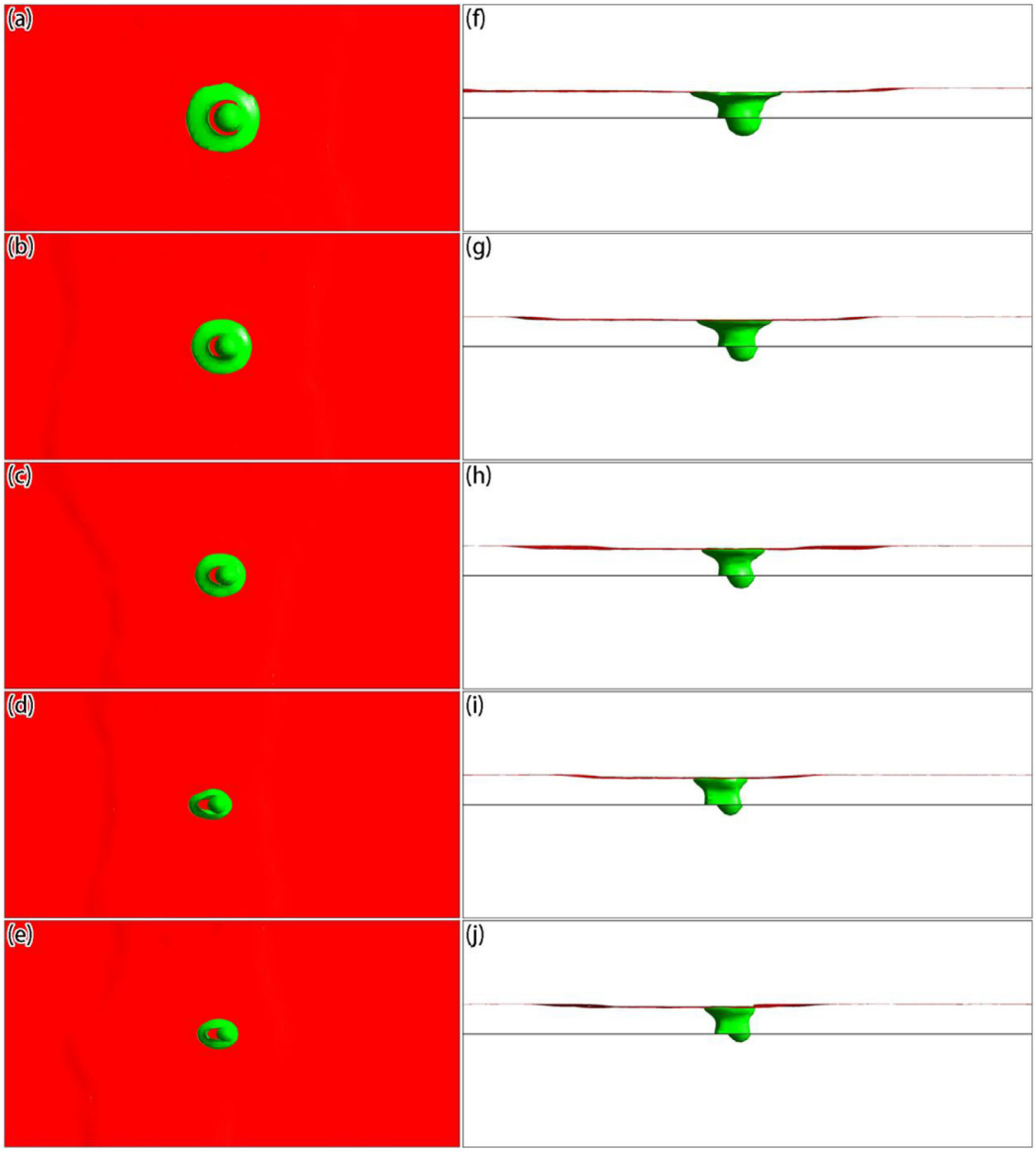

Fig. 15. Bottom view (a∼e) and side view (f∼j) of the liquid surface and molten pool morphology when the laser was applied to the center of the powder layer at different scanning speeds: (a, f) 0.1 m/s; (b, g) 0.2 m/s; (c, h) 0.3 m/s; (d, i) 0.4 m/s; and (e, j) 0.5 m/s.

Table 3
Four calculation schemes to examine the effects of surface tension, Marangoni effect, and gasification recoil force.

Calculation schemes	Laser power (W)	Scanning speed (m/s)	Surface tension considered?	Marangoni effect considered?
A	300	0.1	Yes	Yes
B	300	0.1	No	Yes
C	300	0.1	Yes	No
D	300	0.1	No	No

gradually became concave under the combined influence of the surface tension, the Marangoni effect, and the gasification recoil force (Fig. 8).

Figs. 9 and 10 show the velocity distributions of the liquid surface and the mid-section in Scheme A. Based on the liquid surface velocity, the liquid metal flowed from the center of the molten pool to its periphery under the influence of the Marangoni effect due to the Gaussian distribution of the liquid surface temperature (Fig. 9). Based on the velocity in the mid-section, an annular convection phenomenon about the axial center of the molten pool also occurred in the

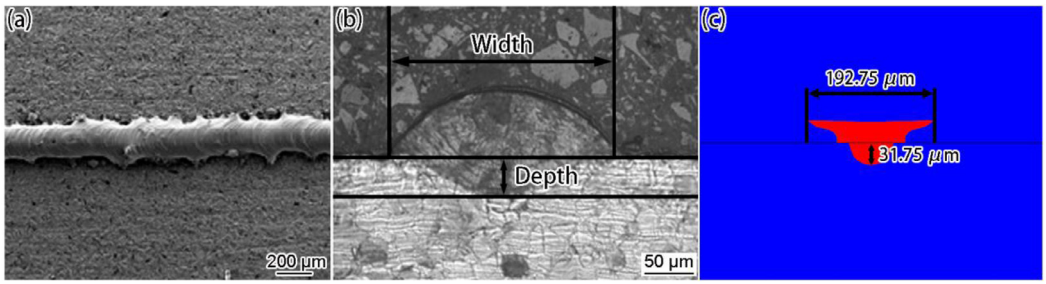

Fig. 16. The experimental [36] and simulation results of the solidified track shape at the scanning speed of 0.1 m/s: (a) experimental result of the surface morphology of the solidified track; (b) experimental result of cross-section morphology of the solidified track; (c) simulation result of cross-section morphology of the solidified track.

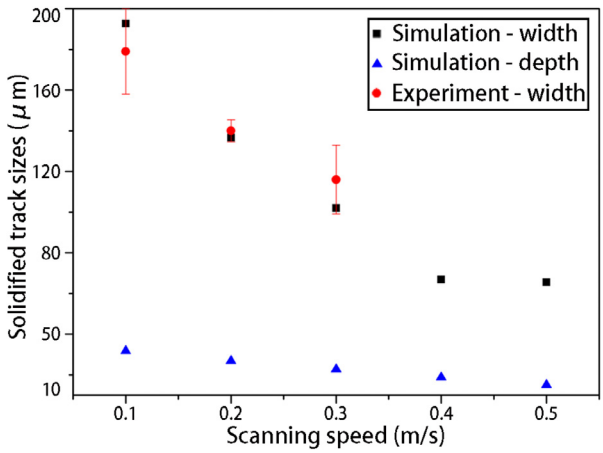

Fig. 17. Solidified track sizes comparison of simulation and experiment [36] at different scanning speeds.

gas phase due to the Marangoni flow on the liquid surface. The tangential flow of the molten pool surface and internal convection affected the morphology of the molten pool (Fig. 10).

To examine the influences of three factors (surface tension, Marangoni effect, and gasification recoil force) on the evolution of the liquid metal surface morphology, the calculated liquid surface morphologies at different times for schemes A, B, C, and D were compared. When the influence of surface tension was not considered, the liquid metal surface in the active laser region sharply depressed as the laser action time increased and the depressed area gradually enlarged. Moreover, the edge of the concave area was significantly higher than the initial position of the surface of the powder layer, resembling a crater (Fig. 11). When the influence of the Marangoni effect was not considered, the liquid metal surface morphology did not show large fluctuations as the active laser time increased, which showed that the surface tension and the gasification recoil force were well balanced in this process (Fig. 12). When the influences of surface tension and the Marangoni effect were neglected simultaneously, as the active laser time increased, the liquid metal surface was sharply depressed under the gasification recoil force. However, the edge of the concave area was not significantly higher than the initial position of the surface of the powder layer (Fig. 13).

In summary, the surface tension stabilized the liquid metal surface, while the Marangoni effect and the gasification recoil force cause the liquid metal surface to appear concave. The difference between the Marangoni effect and the gasification recoil force is that the tangential movement of the liquid metal surface caused by the Marangoni effect causes the molten metal in the central region to accumulate, forming a crater-like liquid surface morphology.

3.3. Effect of scanning speed on SLM process

Fig. 14 shows the liquid surface temperature and local velocity distributions when the laser was applied to the center of the powder layer at different scanning speeds for a laser power of 100 W. As the scanning speed increased, the temperature of the spot area was significantly reduced (Fig. 14a–e), because the action time of the laser at a fixed position was reduced. The local velocity distributions of the liquid metal surface (Fig. 14f–j) showed that as the scanning speed increased, the Marangoni effect weakened and the tangential velocity of the liquid metal on the surface became smaller. The simulation results of the liquid surface and the molten pool morphology at different scanning speeds (Fig. 15) showed that as the

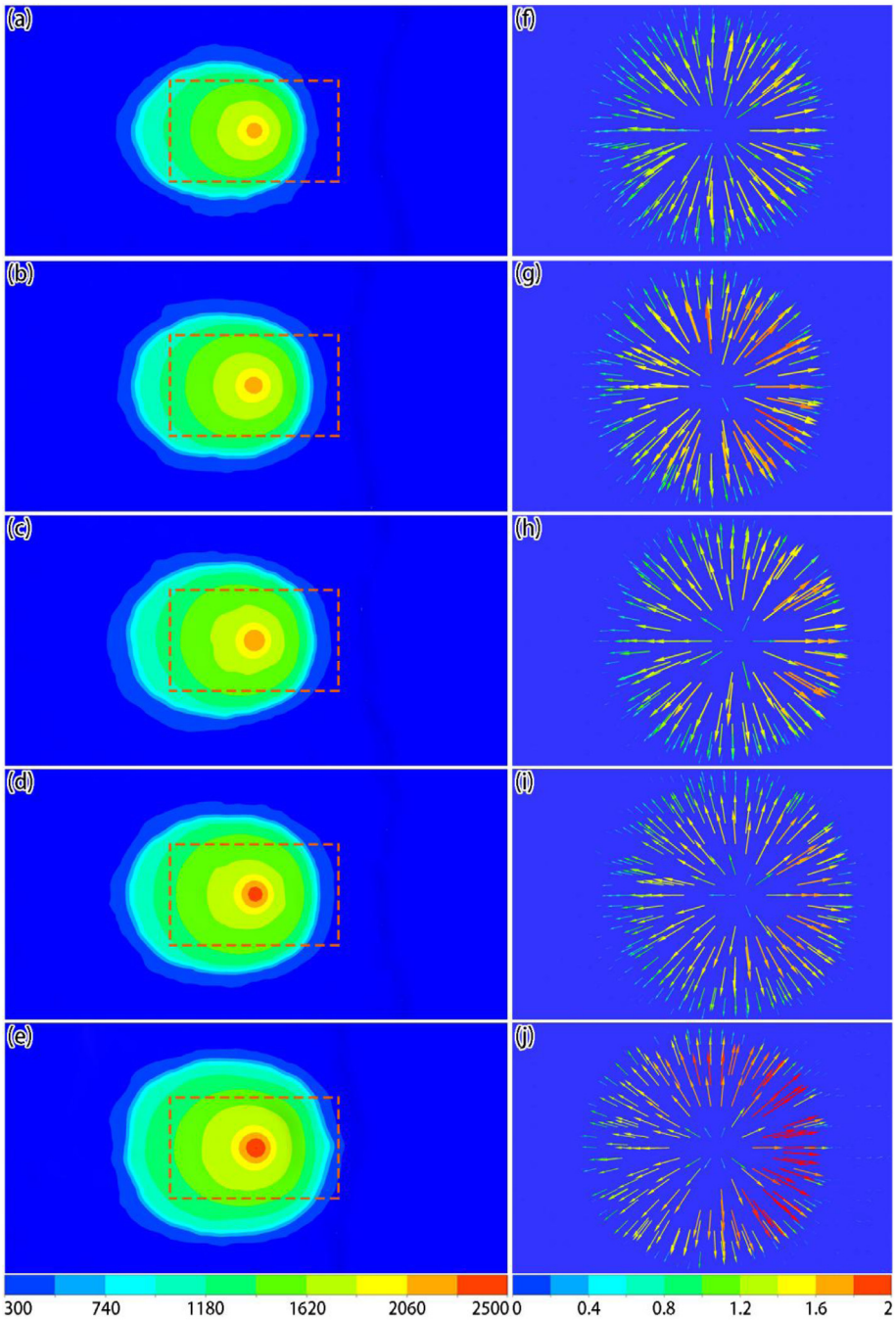

Fig. 18. Liquid surface temperature (a∼e, unit: K) and local velocity (f∼j, unit: m/s) distributions when the laser was applied to the center of the powder layer under different laser powers: (a, f) 80 W; (b, g) 90 W; (c, h) 100 W; (d, i) 110 W; and (e, j) 120 W.

scanning speed increased, the size of the molten pool gradually decreased, but the fluctuations of the liquid metal surface did not change significantly.

Fig. 16 shows the experimental and simulated results of the solidified track shape at a scanning speed of 0.1 m/s. The cross-section of the solidified track obtained experimentally was a semi-elliptical shape, and the upper part of the solidified track was wider than the lower part in the simulation. The reason for this is that the model based on the workpiece scale could not characterize certain motion, such as the collapse of the particles. However, key data of the SLM process can be obtained through the simulation results, namely the solidified track width and depth (as defined in Fig. 16b). The simulated solidified track width was 192.75 μm and the depth was 31.75 μm (Fig. 16c). The experimentally

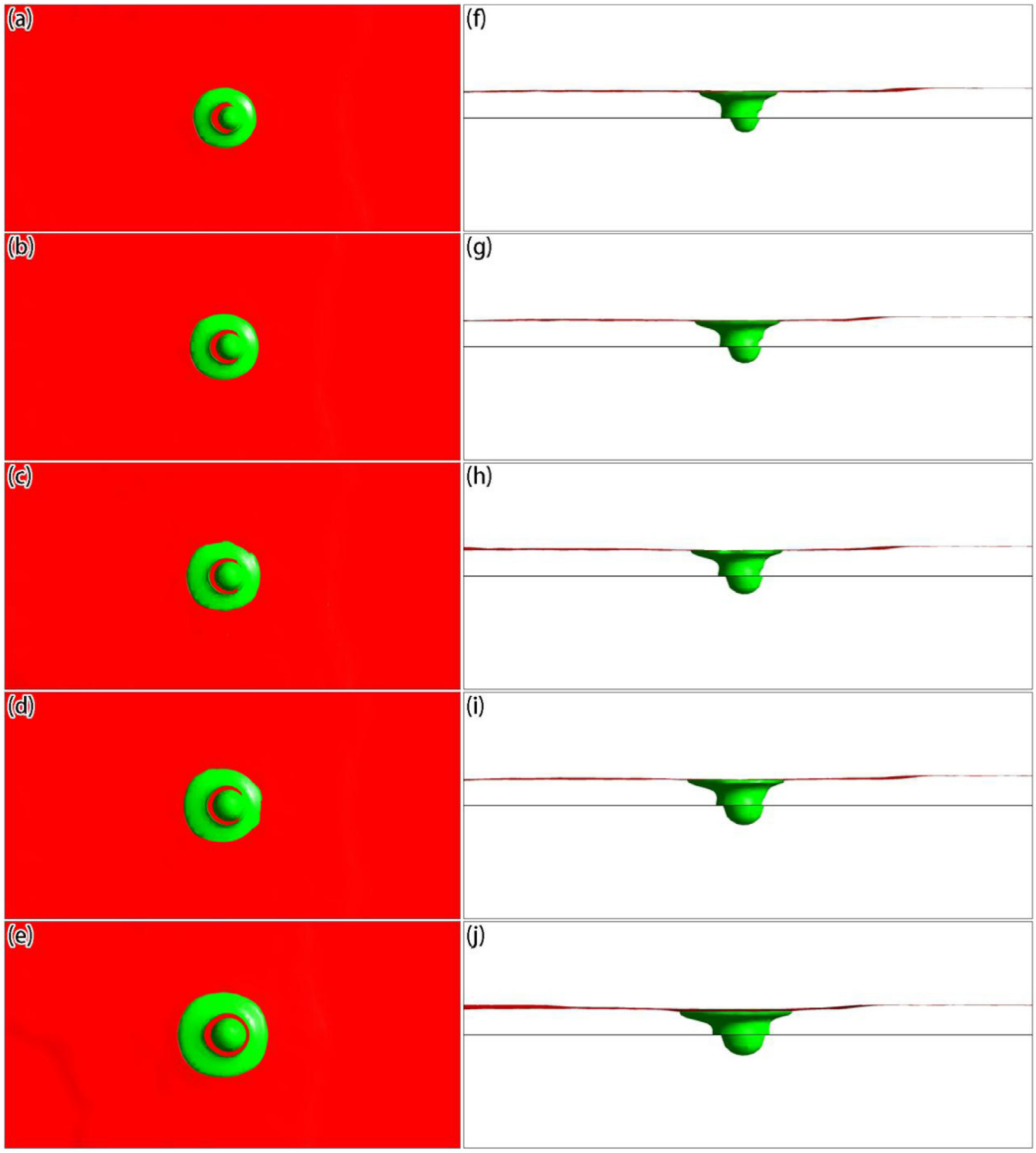

Fig. 19. Bottom view (a∼e) and side view (f∼j) of the liquid surface and molten pool morphology when the laser was applied to the center of the powder layer under different laser powers: (a, f) 80 W; (b, g) 90 W; (c, h) 100 W; (d, i) 110 W; and (e, j) 120 W.

obtained solidified track width was 179 ± 21 μm and the depth was 28±2.95 μm[36]. Thus, the two were in good agreement. Based on the simulated and experimental solidified track size results at different scanning speeds (Fig. 17), as the scanning speed was increased, the width of the solidified track was gradually reduced. When the scanning speed exceeded 0.4 m/s, the rate of the decrease in the molten width with the scanning speed significantly decreased. The depth always decreased linearly with the scanning speed. Therefore, the molten pool dynamic behavior model based on the workpiece scale can be used to describe the SLM process to a certain extent, and the model can feasibly describe the SLM process.

3.4. Effect of laser power on SLM process

Fig. 18 shows the liquid surface temperature and local velocity distributions when the laser was applied to the center of the powder layer under different laser powers for a scanning speed of 0.1 m/s. As the laser power increased, the temperature of the spot area increased significantly (Fig. 18a–e). Based on the local velocity distributions of the liquid metal surface (Fig. 18f–j), as the laser power increased, the Marangoni effect became more apparent, and the tangential

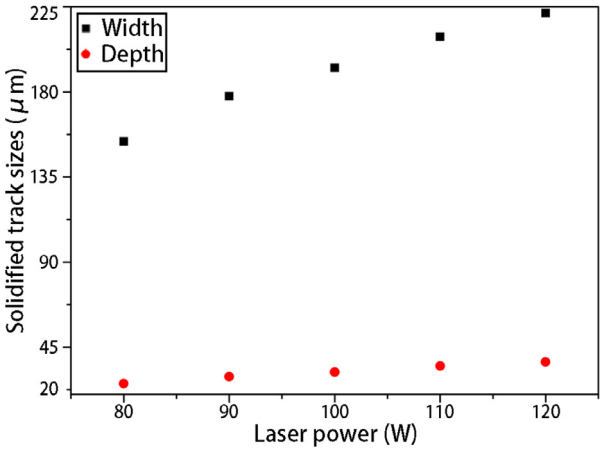

Fig. 20. Comparison of the simulation results for the solidified track sizes under different laser powers.

speed of the liquid metal on the liquid surface became larger. Based on the simulated results of the liquid surface and the molten pool shape under different laser powers (Fig. 19), as the laser power increased, the sizes of the molten pool gradually increased, but the fluctuations of the molten metal surface were not significantly different. Fig. 20 shows the comparison of the simulation results for the solidified track sizes under different laser powers. The width and depth of the solidified track exhibited a linear increase with the laser power.

4. Conclusions

(1) A reasonable and comprehensive model of the SLM process was constructed. Liquid metal gasification pressure and heat dissipation models were established based on the smooth gasification pressure model. To characterize the transformation of the powder layer state (particle, liquid and solid) in the SLM process, the equivalent density, specific heat capacity and thermal conductivity models based on the state were established.

(2) By comparing and analyzing the different calculation schemes, it was found that the surface tension stabilizes the liquid metal surface, while the Marangoni effect and the gasification recoil force cause the liquid metal surface to appear concave. The difference between the Marangoni effect and the gasification recoil force is that the tangential movement of the liquid metal surface caused by the Marangoni effect causes the molten metal in the central region to accumulate, forming a liquid surface morphology that resembles a crater.

(3) The influence of different process parameters (scanning speed and laser power) on the SLM process of 316L stainless steel was calculated and analyzed. The results of the simulation and the experimentally obtained solidified track sizes were in good agreement. As the scanning speed was increased, the width of the solidified track was gradually reduced. When the scanning speed exceeded 0.4 m/s, the rate of decrease of the molten width decreased significantly. The depth always decreased linearly with the scanning speed. The width and depth of the solidified track exhibited a linear increase with the laser power.

Declaration of competing interest

The authors declare that they have no known competing financial interests or personal relationships that could have appeared to influence the work reported in this paper.

Acknowledgments

This research was supported by the Natural Science Foundation of Guangdong Province, China (no. 2019A1515012040), and the Research Platform Construction Funding of Advanced Institute of Engineering Science for Intelligent Manufacturing, Guangzhou University, China.

I thank LetPub (www.letpub.com) for its linguistic assistance during the preparation of this manuscript.

References

[1] J.H. Sun, J.L. Liu, Q.L. Wan, G.F. Wu, Research progress in surface modification of biomedical 316L stainless steel, Mater. Rev. 25 (5A) (2011) 95–98.

[2] A. Yadollahi, N. Shamsaei, S.M. Thompson, D.W. Seely, Effects of process time interval and heat treatment on the mechanical and microstructural properties of direct laser deposited 316L stainless steel, Mater. Sci. Eng. A 644 (2015) 171–183.

[3] D. Wang, C.H. Song, Y.Q. Yang, Y.C. Bai, Investigation of crystal growth mechanism during selective laser melting and mechanical property characterization of 316L stainless steel parts, Mater. Design 100 (2016) 291–299.
[4] A.S. Wu, D.W. Brown, M. Kumar, G.F. Gallegos, W.E. King, An experimental investigation into additive manufacturing-induced residual stresses in 316L stainless steel, Metall. Mater. Trans. A 45 (13) (2014) 6260–6270.
[5] M. Simonelli, C. Tuck, N.T. Aboulkhair, I. Maskery, I. Ashcroft, R.D. Wildman, R. Hague, A study on the laser spatter and the oxidation reactions during selective laser melting of 316L stainless steel, Al-Si10-Mg, and Ti-6Al-4V, Metall. Mater. Trans. A 46 (9) (2015) 3842–3851.
[6] C. Yan, L. Hao, A. Hussein, P. Young, D. Raymont, Advanced lightweight 316L stainless steel cellular lattice structures fabricated via selective laser melting, Mater. Design 55 (2014) 533–541.
[7] J.A. Cherry, H.M. Davies, S. Mehmood, N.P. Lavery, S.G.R. Brown, J. Sienz, Investigation into the effect of process parameters on microstructural and physical properties of 316L stainless steel parts by selective laser melting, Int. J. Adv. Manuf. Technol. 76 (5–8) (2015) 869–879.
[8] Y. Liu, Y.Q. Yang, S.Z. Mai, D. Wang, C.H. Song, Investigation into spatter behavior during selective laser melting of AISI 316L stainless steel powder, Mater. Design 87 (2015) 797–806.
[9] N. Tepylo, X. Huang, P.C. Patnaik, Laser-based additive manufacturing technologies for aerospace applications, Adv. Eng. Mater. (2019) 1900617.
[10] H. Kyogoku, T.T. Ikeshoji, A review of metal additive manufacturing technologies: Mechanism of defects formation and simulation of melting and solidification phenomena in laser powder bed fusion process, Mech. Eng. Rev. 7 (1) (2020) 19–00182.
[11] Y. Zhang, J. Zhang, Modeling of solidification microstructure evolution in laser powder bed fusion fabricated 316L stainless steel using combined computational fluid dynamics and cellular automata, Addit. Manuf. 28 (2019) 750–765.
[12] L. Cao, Mesoscopic-scale simulation of pore evolution during laser powder bed fusion process, Comput. Mater. Sci. 179 (2020) 109686.
[13] H.C. Tran, Y.L. Lo, Heat transfer simulations of selective laser melting process based on volumetric heat source with powder size consideration, J. Mater. Process. Technol. 255 (2018) 411–425.
[14] D.Y. Zhang, P.D. Zhang, Z. Liu, Z. Feng, C.J. Wang, Y.W. Guo, Thermofluid field of molten pool and its effects during selective laser melting (SLM) of Inconel 718 alloy, Addit. Manuf. 21 (2018) 567–578.
[15] Z.K. Wang, M.B. Liu, Dimensionless analysis on selective laser melting to predict porosity and track morphology, J. Mater. Process. Technol. 273 (2019) 116238.
[16] D.D. Gu, M.J. Xia, D.H. Dai, On the role of powder flow behavior in fluid thermodynamics and laser processability of Ni-based composites by selective laser melting, Int. J. Mach. Tool Manuf. 137 (2019) 67–78.
[17] L. Cao, Study on the numerical simulation of laying powder for the selective laser melting process, Int. J. Adv. Manuf. Technol. 105 (5–6) (2019) 2253–2269.
[18] B.Q. Liu, G. Fang, L.P. Lei, W. Liu, A new ray tracing heat source model for mesoscale CFD simulation of selective laser melting (SLM), Appl. Math. Model. 79 (2020) 506–520.
[19] M. Zheng, L. Wei, J. Chen, Q. Zhang, J.Q. Li, S. Sui, G. Wang, W.D. Huang, Surface morphology evolution during pulsed selective laser melting: Numerical and experimental investigations, Appl. Surf. Sci. 496 (2019) 143649.
[20] M. Zheng, L. Wei, J. Chen, Q. Zhang, C.L. Zhong, X. Lin, W.D. Huang, A novel method for the molten pool and porosity formation modelling in selective laser melting, Int. J. Heat Mass Transfer 140 (2019) 1091–1105.
[21] L. Cao, Numerical simulation of the impact of laying powder on selective laser melting single-pass formation, Int. J. Heat Mass Transfer 141 (2019) 1036–1048.
[22] T. Mukherjee, H.L. Wei, A. De, T. DebRoy, Heat and fluid flow in additive manufacturing - Part I: Modeling of powder bed fusion, Comput. Mater. Sci. 150 (2018) 304–313.
[23] L. Cao, X.F. Yuan, Study on the numerical simulation of the SLM molten pool dynamic behavior of a nickel-based superalloy on the workpiece scale, Materials 12 (2019) 2272.
[24] C. Bruna-Rosso, A.G. Demir, B. Previtali, Selective laser melting finite element modeling: Validation with high-speed imaging and lack of fusion defects prediction, Mater. Design 156 (2018) 143–153.
[25] Y. Liu, J. Zhang, Z.C. Pang, Numerical and experimental investigation into the subsequent thermal cycling during selective laser melting of multi-layer 316L stainless steel, Opt. Laser Technol. 98 (2018) 23–32.
[26] H.K. Versteeg, W. Malalasekera, An Introduction to Computational Fluid Dynamics: The Finite Volume Method, second ed., Pearson education, UK, 2007.
[27] L. Cao, F. Sun, T. Chen, Z.H. Teng, Y.L. Tang, D.M. Liao, Numerical simulation of liquid-solid conversion affecting flow behavior during casting filling process, Acta Metall. Sin. 53 (11) (2017) 1521–1531.
[28] J.U. Brackbill, D.B. Kothe, C. Zemach, A continuum method for modeling surface tension, J. Comput. Phys. 100 (2) (1992) 335–354.
[29] J. Yang, F. Wang, 3D finite element temperature field modelling for direct laser fabrication, Int. J. Adv. Manuf. Technol. 43 (11–12) (2009) 1060–1068.
[30] C.W. Hirt, B.D. Nichols, Volume of fluid (VOF) method for the dynamics of free boundaries, J. Comput. Phys. 39 (1) (1981) 201–225.
[31] L. Cao, D.M. Liao, Y.L. Zhang, T. Chen, Heat transfer model of directional solidification by LMC process for superalloy casting based on finite element method, Metall. Mater. Trans. A 47 (9) (2016) 4640–4647.
[32] G.X. Xu, C.S. Wu, C.L. Qin, X.Y. Wang, S.Y. Lin, Adaptive volumetric heat source models for laser beam and laser + pulsed GMAW hybrid welding processes, Int. J. Adv. Manuf. Technol. 57 (2011) 245–255.
[33] C. Panwisawas, C.L. Qiu, M.J. Anderson, Y. Sovani, R.P. Turner, M.M. Attallah, Mesoscale modelling of selective laser melting: Thermal fluid dynamics and microstructural evolution, Comput. Mater. Sci. 126 (2017) 479–490.
[34] S.Y. Pang, K. Hirano, R. Fabbro, T. Jiang, Explanation of penetration depth variation during laser welding under variable ambient pressure, J. Laser Appl. 27 (2) (2015) 022007.
[35] K. Dai, L. Shaw, Thermal and mechanical finite element modeling of laser forming from metal and ceramic powders, Acta Mater. 52 (1) (2004) 69–80.
[36] A. Masmoudi, R. Bolot, C. Coddet, Investigation of the laser-powder-atmosphere interaction zone during the selective laser melting process, J. Mater. Process. Technol. 225 (2015) 122–132.